Optimization of a Broadband Lithium Niobate-Barium Titanate Hybrid Modulator With Low Half-Wave-Voltage-Length Product

Ahmed Shariful Alam and J. Stewart Aitchison, *Fellow, IEEE*

***Abstract*—The Electro-optic (EO) modulator is one of the most important devices for optical communication. Lithium niobate on insulator (LNOI) platform has matured over the last few years and has resulted in some excellent EO modulators with very low voltages, low optical losses, and high bandwidth. In this paper, we proposed a novel EO modulator based on the LNOI platform where a cladding material of very high dielectric constant i.e., barium titanate (BTO) is used around an etched lithium niobate (LN) waveguide. Lumerical Mode and Device simulations have been used to optimize a Mach-Zehnder interferometer (MZI) based EO modulator that shows a half-wave-voltage-length product as low as ∼1.36 V.cm maintaining the optical loss due to metal absorption of ∼1 dB/cm. The 3 dB EO bandwidth of ∼132 GHz has been estimated using the data generated by the microwave simulations carried out in CST Studio Suite.**

***Index Terms*—High-K dielectric, lithium niobate modulator, half-wave-voltage-length product, broadband modulator.**

I. Introduction

HIGH-SPEED and energy efficient Electro-optic (EO) modulators are key components for high-capacity optical fiber communications [1]. Since the early days of optical communications, lithium niobate (LN) has been one of the most used materials for very high-speed EO modulators due to a combination of high EO coefficient (r_{33} = 31 pm/V) and wide transparency window (340–4600 nm). Nevertheless, conventional LN modulators are based on low index contrast (Δn∼0.02) LN waveguides fabricated by titanium in-diffusion [2]. Hence, these waveguides have large optical modes leading to power hungry, bulky modulators with high operating voltages. However, for short-reach optical communication systems, more power efficient i.e., chip-scale compact modulators are required. Though many integrated devices with low optical loss and low operating voltage have been demonstrated in silicon [3], [4], silicon-polymer hybrid [5], [6], [7], III-V compound semiconductor [8], [9] and epsilon-near-zero (ENZ) [10], [11], [12] platforms, but none of them could achieve high modulation bandwidth available with LN modulators. A specific type of ENZ platform-based modulator, the plasmonic-organic hybrid (POH) modulator, surpassed the bandwidth of LN modulators, but suffers from high optical loss due to metal absorption [13], [14].

Thin film LN (TFLN) fabricated by crystal ion slicing and wafer bonding [15] enables the LNOI platform to offer some excellent chip-scale modulators with low optical loss, low driving voltage and very high EO bandwidth. These TFLN modulators have very low footprint due to the high refractive index contrast LN rib waveguides which can exhibit extremely low optical scattering loss (as low as ∼ 0.03 dB/cm) due to the very smooth waveguide sidewall roughness using dry etching of TFLN [16]. Uniform coplanar waveguides (CPW) have been used for the first generation TFLN modulators which achieved half-wave-voltage-length product ($V_\pi L$) in the range of ∼2.2 V.cm. The electrodes of the CPW are placed far away from the LN rib waveguides so that the simulated values of optical loss due to metal absorption remain below 0.03 dB/cm. Though longer devices have lower half-wave-voltage (V_π), the 3-dB EO bandwidth is quite low because of the RF transmission loss. A 5 mm device has a (V_π) of 4.4 V and a 3-dB EO bandwidth of 100 GHz, whereas a 20 mm device has a (V_π) of 1.4 V and a 3-dB EO bandwidth of 45 GHz [17]. Therefore, in order to enhance the bandwidth of the TFLN modulators, reducing the $V_\pi L$ is necessary. One way to do that is to increase the etch depth of LN so that the electrodes can be placed closer to the LN waveguide maintaining the same optical loss due to metal absorption. However, this approach may increase the scattering loss at the LN waveguide sidewalls because of higher etch depth. Another way is to replace the uniform CPW with travelling wave electrodes (TWE) which was done during the fabrication of second generation of TFLN modulators. Although the use of TWE increases the 3-dB EO bandwidth of the device by reducing the RF transmission loss, it does not reduce the $V_\pi L$ of the device. The 3-dB EO bandwidth of 20 mm TFLN modulator with TWE is expected to have a 3-dB EO bandwidth beyond 100 GHz whereas the V_π of the device remains ∼1.35 V which is almost the same as the V_π of the TFLN modulator with uniform CPW [18]. We previously reported a new approach to optimize the $V_\pi L$ by using a cladding material with very high dielectric constant, such as BTO around the LN waveguide [19]. Other reports have suggested magnesium oxide (MgO) as the high dielectric constant cladding material [20]. Generally, in

Manuscript received 23 July 2023; revised 24 October 2023; accepted 31 October 2023. Date of publication 3 November 2023; date of current version 16 November 2023. This work was supported by the Natural Sciences and Engineering Research Council (NSERC) Discovery under Grant RGPIN-2022-04871. *(Corresponding author: Ahmed Shariful Alam.)*

The authors are with the Department of Electrical & Computer Engineering, University of Toronto, Toronto, ON M5S1A4, Canada (e-mail: as.alam@mail.utoronto.ca; stewart.aitchison@utoronto.ca).

Digital Object Identifier 10.1109/JPHOT.2023.3329781

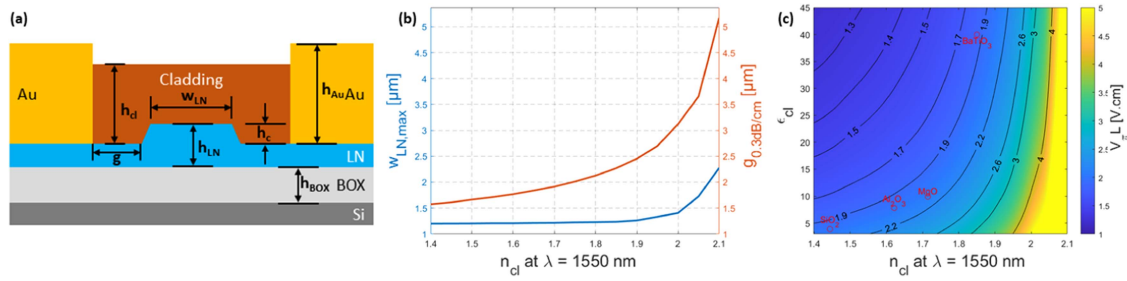

Fig. 1. (a) Cross-sectional view of TFLN based modulator. All the thicknesses are adapted from ref. [17], LN waveguide core, w_{LN} widths are maximized maintaining the single mode condition ($w_{LN,max}$) and the gap between the waveguide core and the metal electrode, g is minimized to achieve a loss just lower than 0.3 dB/cm ($g_{0.3\,dB/cm}$). (b) Change of $w_{LN,max}$ and $g_{0.3\,dB/cm}$ with respect to the change of cladding material's refractive index, n_{cl} at 1550 nm wavelength. (c) Colormap of 1401 × 1401 $V_\pi L$ matrix calculated by cubic interpolation of the previously calculated 15 × 15 $V_\pi L$ matrix with a contour of different $V_\pi L$ values. The prospect of different cladding materials such as SiO_2, MgO, Al_2O_3 and $BaTiO_3$ are benchmarked on this $V_\pi L$ colormap.

state-of-the-art TFLN modulators SiO_2 is used as a cladding material which ensures very high confinement of the optical mode in the core of LN rib waveguide; however, SiO_2 fails to confine the RF electric field within the LN core region. In this work we proposed a new TFLN modulator loaded with a high-K material, BTO cladding which not only improves the RF electric field confinement in the LN core, but also ensures the optical confinement in the LN core region because of the low refractive index of sputter deposited BTO. In our previous work we showed by simulation that an ultra-low $V_\pi L$ of ∼1.52 V.cm can be achieved maintaining a loss below 0.3 dB/cm due to the metal absorption [19]. Additionally, we did a $V_\pi L$ mapping considering different refractive indices and dielectric constants which will allow us to choose the right cladding material to get an overall $V_\pi L$ improvement. We also showed the design of CPW in order to minimize the RF mode propagation loss & RF insertion loss and estimated the 3-dB EO bandwidth of the proposed modulator. Since our first proposal [19] etched TFLN modulators with a composite cladding consist of a SiO_2 layer and a high dielectric constant liquid overlayer have been demonstrated [21], our optimized device shows better performance.

II. RF Electric Field Confinement Depending on Cladding Material Properties

High confinement of both the optical mode and the RF electric field within the core region of the LN rib waveguide are necessary for the best device performance. Hence, an ideal cladding material should have a very low refractive index at 1550 nm wavelength and a very high dielectric constant in the RF domain. Before diving into the comparison of different cladding materials we established a colormap showing $V_\pi L$ for different refractive indices and dielectric constants considering a modulator structure similar to Fig. 1(a). All the dimensions such as the thickness of the LN layer (c), the LN etch depth (h_c), the metal layer thickness (h_{Au}), the cladding thickness (h_{cl}) and the BOX layer thickness (h_{BOX}) are considered same as ref. [17] i.e., h_{LN}, h_c, h_{Au}, h_{cl} and h_{BOX} are considered 600 nm, 300 nm, 1.1 μm, 800 nm and 4.7 μm respectively. The sidewall angle of the waveguide core is 65°. A refractive index sweep of the cladding material (n_{cl}) was done from 1.4 to 2.1 with a step size of 0.05. For each n_{cl} the LN waveguide core width (w_{LN}) is maximized ($w_{LN,max}$) in such a way that the waveguide supports only the fundamental TE mode. All the values of n_{cl} are considered for 1550 nm wavelength. The blue curve of Fig. 1(b) shows the $w_{LN,max}$ with the change n_{cl} at 1550 nm wavelength. Waveguides with core widths less than $w_{LN,max}$ support only the fundamental TE mode, but for smaller core widths the evanescent tail in the cladding region will expand further away from the core region which will limit the gap between the metal layer and the waveguide core (g). For each set of n_{cl} and $w_{LN,max}$ the gap, g is minimized ($g_{0.3\,dB/cm}$) in such a way that the optical loss due to the metal absorption remains just below 0.3 dB/cm. The red curve of Fig. 1(b) shows the change of $g_{0.3\,dB/cm}$ with the change n_{cl} at 1550 nm wavelength. For each set of n_{cl}, $w_{LN,max}$ and $g_{0.3\,dB/cm}$ a sweep of DC dielectric constant of the cladding material (ϵ_{cl}) has been done from 3 to 45 with a step size of 3 in order to calculate the $V_\pi L$. Thus, a 15 × 15 matrix of $V_\pi L$ was calculated for all combinations of n_{cl} and ϵ_{cl}. Next a cubic interpolation of the 15 × 15 $V_\pi L$ is carried out to convert this into a 1401 × 1401$V_\pi L$ matrix which is depicted in a colormap in Fig. 1(c). Fig. 1(c) also includes the contour lines of different $V_\pi L$ and shows where different cladding materials such as SiO_2, MgO, Al_2O_3, $BaTiO_3$. $BaTiO_3$ (with n_{cl} = 1.85 [6] and ϵ_{cl} = 40 [7]) sits on the left side of the 1.9 V.cm $V_\pi L$ contour line whereas SiO_2 (with n_{cl} = 1.4431 [22] and ϵ_{cl} = 3.9 [23]), MgO (with n_{cl} = 1.7146 [24] and ϵ_{cl} = 9.9 [25]) and Al_2O_3 (with n_{cl} = 1.6216 [22] and ϵ_{cl} = 7.8 [26]) on the right side of 1.9 V.cm $V_\pi L$ contour line. Therefore, it is clear that $BaTiO_3$ is a better cladding material than other aforementioned materials in order to achieve a lower $V_\pi L$.

III. LN-BTO Hybrid Modulator

A. Waveguide Structure Optimization

According to Fig. 1(c), BTO shows better potentiality as a cladding material. Hence, we moved forward with the LN-BTO Hybrid Modulator. The use of BTO as a cladding material greatly enhances the static electric confinement within the LN waveguide core region. However, the optical confinement within the LN core region is compromised due to the lower refractive index contrast between LN (2.21) and BTO (1.85) [6] at 1550 nm

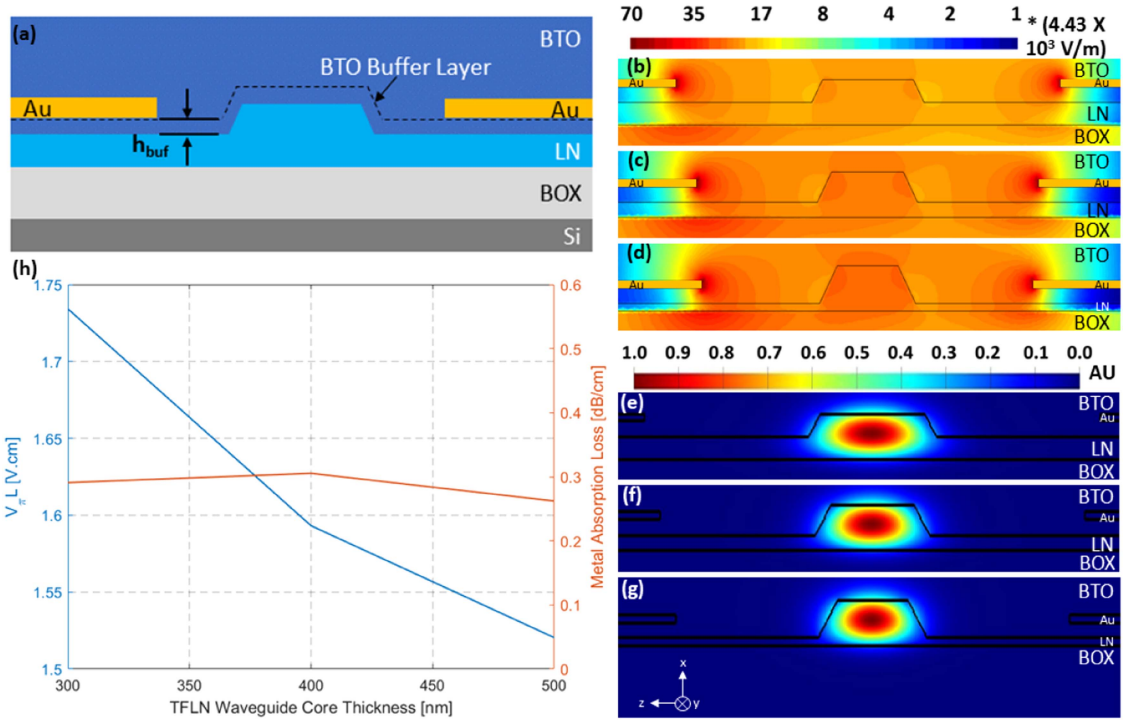

Fig. 2. (a) Cross-sectional view of LN-BTO Hybrid Modulator with $h_{buf} = 200$ nm. Lumerical Device simulations for the static electric field distribution ($|E_{z,elec.}|$) considering (b) $h_c = 300$ nm, (c) $h_c = 400$ nm & (d) $h_c = 500$ nm respectively. The scale of electric field is normalized to 4.43×10^3 V/m. Lumerical Mode simulations for the electric field intensities ($|E_{z,opt}|^2$) for the optical modes considering (e) $h_c = 300$ nm, (f) $h_c = 400$ nm & (g) $h_c = 500$ nm respectively. (h) Change of $V_\pi L$ and metal absorption loss of the optimized structure with the change of TFLN waveguide core thickness.

which eventually increases the chance of higher optical metal absorption loss. Hence, the waveguide structure i.e., the LN etch depth, h_c, the gap between the LN core and the metal electrode, g, the metal electrode thickness, h_{Au} etc. need to be optimized to realize an efficient LN-BTO hybrid modulator. In our previous work [19], we showed a cross-sectional view of the LN-BTO hybrid modulator like Fig. 2(a). In that structure we considered an additional buffer BTO layer with a thickness, h_{buf} between the LN slab and Au electrodes since it was observed previously that such a buffer dielectric layer is able to reduce the optical loss due to the metal absorption to some extent [27].

We start the optimization process by considering the LNOI wafer stack of x-cut LN/BOX (buried oxide)/Silicon (Si) where the LN, BOX and Si layers have a thickness of 600 nm, 4.7 μm and 500 μm respectively. Other device thicknesses such as, the electrode layer thickness, h_{Au}, and the BTO buffer layer thickness, h_{buf} are considered to be 100 nm and 200 nm respectively. The sidewall angle of the LN waveguide core is 65°. Initially we consider the etch depth of LN waveguide core, h_c to be 300 nm. For this core height a core width, $w_{LN} = 1.2$ μm will ensure the dominant single TE mode operation. The gap between the Au electrode and the LN waveguide core edge, g ~1.8 μm (metal to metal gap of ~5 μm) was found to give a metal absorption just below ~0.3 dB/cm. The simulated value of the $V_\pi L$ of this modulator is ~1.73 V.cm which shows ~21% improvement than ref. [17]. In the earlier report [19], we further extended the simulations by considering LN core thicknesses of 400 nm and 500 nm. For single mode operation, 950 nm & 800 nm of LN core top surface widths were chosen and ~4.6 μm & ~4.3 μm metal to metal gaps were chosen so that metal absorption loss remains below 0.3 dB/cm for the respective LN core thicknesses. Fig. 2(b), and (c) show the static electric field distributions for LN core thicknesses of 300 nm, 400 nm & 500 nm respectively when 0.5 V is applied between the two electrodes placed on two sides of the LN waveguide core. Fig. 2(e)–(g) show the TE optical mode field distribution at 1550 nm wavelength for the respective LN core thicknesses. For 400 nm and 500 nm LN core thicknesses the $V_\pi L$ was calculated to be ~1.59 V.cm and ~1.52 V.cm respectively maintaining the optical losses below 0.3 dB/cm margin that is depicted in Fig. 2(h). Therefore, it is possible to reduce the $V_\pi L$ of the device by etching LN more whereas the optical scattering loss due to the sidewall roughness the of the LN waveguide is expected to be low because the refractive index contrast is comparatively higher when BTO cladding is used. As a next step, we simulate the optical loss due to metal absorption (solid lines) as well as the $V_\pi L$ (broken lines) of an LN-BTO hybrid modulator for different BTO buffer thicknesses which is shown in Fig. 3(a). It was noticed that, for 300 nm LN core thickness the optical loss (solid blue line) due to metal absorption sharply decreases up to 200 nm BTO buffer layer thickness. If the thickness of the BTO buffer layer is further increased, the optical loss decreases very slowly. This happens because after 200 nm of BTO buffer thickness the top surface of the metal layer goes above the top surface of the LN

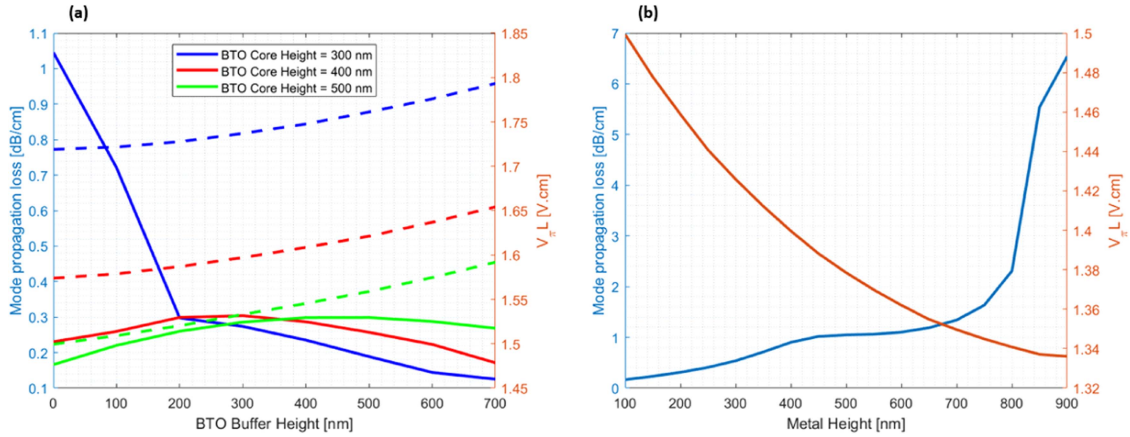

Fig. 3. (a) Change of optical absorption loss and $V_\pi L$ with the change of BTO buffer layer thickness, h_{buf} for different LN core thicknesses, h_c. (b) The change of optical absorption loss and $V_\pi L$ with the change of metal electrode thickness, h_{Au} considering $h_c = 500$ nm and $h_{buf} = 0$ nm. All the results were obtained from the Lumerical Mode and Device simulations.

core and the overlap of the optical mode with the metal layer reduces. Thus, the inclusion of a buffer cladding layer between the metal electrodes and the LN slab layer reduces the optical loss as claimed in ref. [27]. For higher LN core thicknesses this is not entirely true. As for example, for 400 nm & 500 nm LN core thicknesses the optical losses (solid red & green lines respectively) increase up to 300 nm & 500 nm of BTO buffer layer thicknesses respectively and start to reduce after these thicknesses respectively. The behavior of the optical absorption loss can be explained by the fact that, for higher LN etch depths the confinement of the optical mode in the LN slab region reduces and the evanescent wave is exposed more in the BTO cladding region. Therefore, increasing the BTO buffer layer thickness exposes the metal layer more towards the evanescent wave of the optical mode in the BTO cladding region. For BTO buffer layer thicknesses greater than 300 nm and LN waveguides with thicknesses of 400 nm the metal electrode losses become negligible. For all LN core thicknesses, the $V_\pi L$ (broken blue, red & green lines) increase monotonously with the increase of BTO buffer layer thickness. Hence, in the subsequent simulation we fix the LN core thickness at 500 nm. We also avoid having any BTO buffer layer since this not only increases the optical loss for higher LN etch depths but also increases the fabrication complexity.

Next, we simulate the LN-BTO hybrid modulator to get the optical losses and $V_\pi L$ for different metal electrode thicknesses. Fig. 3(b) shows that the optical absorption loss increases slowly when the metal electrode thickness is increased from 100 nm to 400 nm. The optical loss remains almost the same ($\sim$1 dB/cm) until the metal thickness reaches up to 600 nm. After 600 nm of metal thickness the optical loss increases sharply. The $V_\pi L$ reduces almost linearly with the increase of the metal electrode thickness. Considering both the optical loss and the $V_\pi L$ curves an optimum metal thickness of 600 nm is chosen so that the optical loss remains near $\sim$1 dB/cm and a $V_\pi L$ of $\sim$1.36 V.cm can be achieved. To the best of our knowledge, this is the lowest $V_\pi L$ value for all LNOI based modulators. The cross-sectional view of the optimized LN-BTO hybrid modulator looks like Fig. 4(a). Fig. 4(b) shows the static electric field distribution of the optimized device when 0.5 V is applied between the two electrodes placed on two sides of the LN waveguide core and Fig. 4(c) shows the optical mode field distribution of the optimized modulator at 1550 nm wavelength.

B. Transmission Lines Design and Bandwidth Estimation

Once the waveguide structure is optimized for the best possible tradeoff between the optical loss and $V_\pi L$, we can turn our attention towards the transmission line i.e., the coplanar waveguide (CPW) design. The RF electrical field is applied using a ground-signal-ground (GSG) transmission line. A CPW with infinite ground width has several advantages such as, low dispersion, low radiation loss, suppression of parasitic RF modes etc. A CPW having two to three times the ground width compared to the central conductor width acts very similar to a CPW with infinite width ground electrodes [28]. The RF electric field is well confined between the center and ground electrodes, especially with the LN waveguide core, which can be seen from the RF electric mode field distribution at 10 GHz shown in Fig 5(a). To account for the conformal deposition of BTO we have added BTO regions above the Au electrodes. This CPW structure is broadband and optimized for 50 Ω having a center electrode width, s = 2.05 μm and ground electrode width, g = 4.11 μm. Fig. 5(c) shows magnitude of the S-parameters, $|S_{11}|^2$ and $|S_{21}|^2$ in dB which quantify the reflected and the transmitted power respectively through the designed CPW for a modulator length, L of 500 μm. The S-parameters were generated by using the Time Domain solver of the FDTD simulation tool, CST Microwave Studio (CST MWS). Frequency independent dielectric constants of LN and BTO are considered as 28 and 40 respectively which are same as the values considered while doing the DC electric field distribution simulations using the Lumerical Device module. The eigen mode solution for the fundamental RF mode provides the broadband characteristic impedance that is shown in Fig. 6(a). The characteristics impedance of the designed CPW is very well matched to 50 Ω over a very broad range

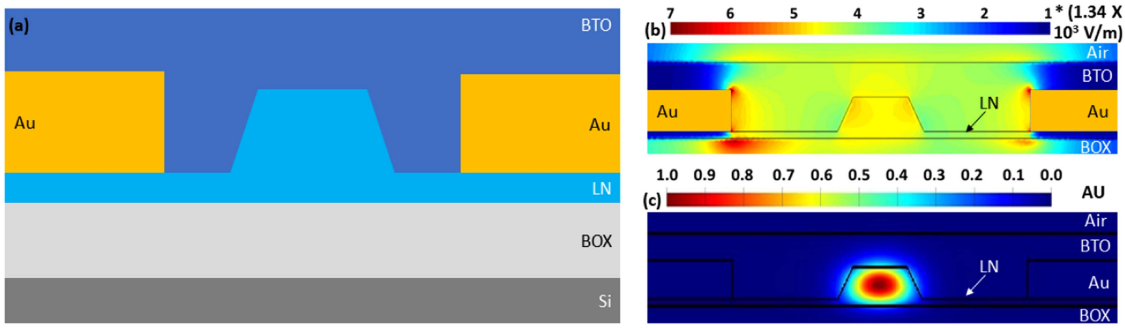

Fig. 4. (a) Cross-sectional view of optimized LN-BTO Hybrid Modulator. (b) Lumerical Device simulation for the static electric field distribution of the optimized waveguide region of an LN-BTO hybrid modulator. considering $h_c = 500$ nm, $h_{buf} = 0$ nm, and $h_{Au} = 600$ nm. The scale of electric field is normalized to 1.34×10^3 V/m. (c) Lumerical Device simulation for the electric field intensities for the optical mode of the optimized waveguide region of an LN-BTO hybrid modulator considering $h_c = 500$ nm, $h_{buf} = 0$ nm, and $h_{Au} = 600$ nm.

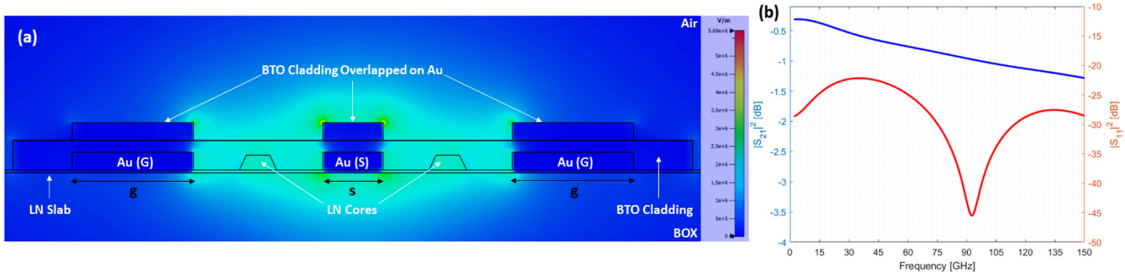

Fig. 5. (a) CST simulation for the RF mode field distribution of the LN-BTO hybrid modulator at 10 GHz considering $s = 2.05$ μm and $g = 4.11$ μm which ensured the 50 Ω broadband characteristic impedance. (b) CST generated S-parameters ($|S_{11}|^2$ & $|S_{21}|^2$) of the of the designed LN-BTO hybrid modulator considering $s = 2.05$ μm and $g = 4.11$ μm.

of frequency which reduces the reflection. The CST generated S-parameter can be used to extract the complex propagation constant, γ. The imaginary part of the of the complex S_{21} is the propagation constant, β that can be used to get the microwave effective index, n_{mw} using the expression, $\beta = \frac{2\pi f_{RF}}{c} n_{mw}$. The microwave effective indices over a broad frequency range shown in Fig. 6(b) are not well matched with the optical group refractive index ($n_{opt} = 2.18$) at 1550 nm wavelength. The real part of the complex S_{21} gives us the attenuation constant, α of the microwave signal, which is shown in Fig. 6(c). The index matching between the microwave mode and the optical mode as well as the reduction of the microwave loss can be performed by designing a segmented coplanar waveguide which is beyond the scope of this paper [18].

The simulated values of attenuation coefficient, α and the microwave refractive indices, n_{mw} over a broad frequency range have been used to calculate the electro-optic response of the designed LN-BTO hybrid modulator. Theoretically the bandwidth of the electro-optic response can be calculated by [29]:

$$M(f_{RF}) = 20\log\left[e^{\frac{-\alpha L}{2}}\left\{\frac{\sinh^2\left(\frac{\alpha L}{2}\right) + \sin^2\left(\frac{bL}{2}\right)}{\left(\frac{\alpha L}{2}\right)^2 + \left(\frac{bL}{2}\right)^2}\right\}^{\frac{1}{2}}\right] \quad (1)$$

Here, b is defined by the expression, $b = \frac{2\pi f_{RF}}{c}(n_{mw} - n_{opt})$ that quantifies the effect of velocity mismatch between the optical and RF mode on the electro-optic bandwidth of the modulator. The electro-optic response of the modulator is shown in Fig. 6(d). The electro-optics response of the modulator shows that the 3 dB cut-off frequency or the 3 dB bandwidth of the designed modulator is expected to be around ∼132 GHz.

TABLE I
COMPARISON OF DIFFERENT ETCHED TFLN MODULATORS IN THE LITERATURE

Ref.	Cladding Material	Etch Depth	$V_\pi L$	Optical Loss	EO Bandwidth
[32]	UV15	1.3 μm	9.4 V.cm	1 dB/cm	40 GHz
[17]	SiO_2	300 nm	2.2 V.cm	0.2 dB/cm	100 GHz
[30]	Air	180 nm	2.2 V.cm	0.98 dB/cm	>70 GHz
[29]	SiO_2	300 nm	1.75 V.cm	0.7 dB/cm	>40 GHz
[31]	SiO_2	300 nm	1.32 V.cm	2.7 dB/cm	>3 GHz
[19]	$BaTiO_3$	500 nm	1.52 V.cm	0.3 dB/cm	–
[21]	SiO_2+ Glycerol	200 nm	1.41 V.cm	1.25 dB/cm	>40 GHz
This work	$BaTiO_3$	500 nm	1.36 V.cm	1 dB/cm	132 GHz

IV. COMPARISON OF ETCHED TFLN MODULATORS

The performances of the state-of-the-art etched TFLN modulators with uniform CPW electrodes are summarized in Table I. Most of these modulators have used low dielectric constant materials like air [30], SiO_2 [17], [29], [31] or UV15 [32]. For the first time, we proposed a TFLN modulator which exploited a high dielectric constant material like BTO [19] as a cladding material which showed significant reduction of $V_\pi L$ with low optical loss. In this paper, we have further reduced the $V_\pi L$ to

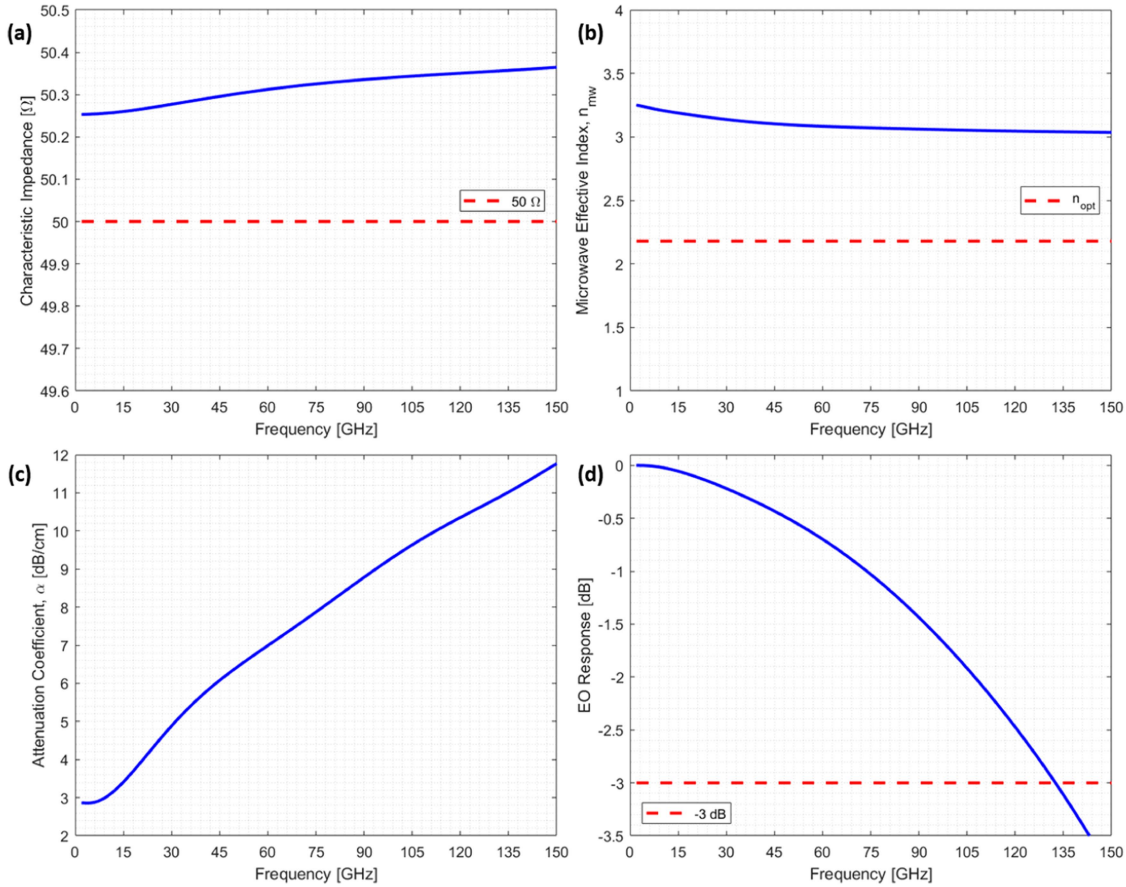

Fig. 6. (a) Broadband characteristic impedance generated by eigne mode simulation in CST of the designed LN-BTO hybrid modulator considering s = 2.05 μm and g = 4.11 μm. (b) Microwave effective index, n_{mw} and (c) attenuation coefficient, α extracted from the S-parameters generated by 3D FDTD simulation in CST. (d) Electro-optics response of the designed LN-BTO hybrid modulator with uniform CPW.

1.36 V.cm for and optical loss less than 1 dB/cm by optimizing multiple physical parameters. Very soon after presenting our first proposal [19], a composite cladding consist of a SiO_2 and a high dielectric constant material like (MgO, Al_2O_3 or Glycerol) has been used in etched TFLN modulators [21]. Although this is a similar concept to our work, the device structure is completely different. However, BTO this films are more suitable than the liquid Glycerol for practical applications. Besides, our optimized structure estimates lower $V_\pi L$ ($\sim$1.36 V.cm), lower optical propagation loss ($\sim$1 dB/cm) and higher EO bandwidth ($\sim$132 GHz) compared to the modulator reported in ref. [21].

V. Conclusion

To summarize, we report the design of an optimized LN-BTO hybrid modulator where the SiO_2 cladding of a conventional thin film LN based modulator with etched LN rib waveguide is replaced with a cladding material with very high-dielectric constant. Using a LN rib waveguide realized by etching LN by 500 nm on a 600 nm thin film LN layer in the LN-BTO hybrid modulator, a $V_\pi L$ of $\sim$1.36 V.cm with an optical loss as low as $\sim$1 dB. To the best of our knowledge this is the lowest $V_\pi L$ values for a thin film LN based modulator. A CPW of 600 nm thick Au layer has been optimized for 50 Ω to reduce the reflection of the RF signal at the point of insertion. Despite velocity mismatch between the optical and RF modes the modulator is expected to have a 3 dB bandwidth beyond 100 GHz (theoretical $f_{3\,dB}$ of $\sim$132 GHz) because of the device length as short as a 500 μm with low RF loss. A longer device can be realized by tuning the BTO cladding thickness and by designing a segmented coplanar waveguide to mitigate the velocity mismatch between RF and optical modes.

Compared to the conventional LNOI based modulators, the main challenges faced by the proposed LN-BTO hybrid modulator lie in two major things – the quality of BTO film for desired optical & RF properties during deposition and the patterning of thicker BTO film. Firstly, high-quality stoichiometric crystalline BTO thin film can be deposited by molecular beam expitaxy (MBE) [33], [34] or metal-organic chemical vapour deposition (MOCVD) [35] method which can provide dielectric constant as high as 2200. But, such films generally have higher refractive index (n_{BTO} = 2.286) as well in the telecommunication wavelengths which can jeopardize the optical confinement in the LN waveguide core region [34]. Moreover, the above-mentioned deposition methods may require very high deposition temperature (up to 900°C) which is not compatible with pre-existing metal layers. On the other hand, amorphous BTO thin films can be deposited by RF magnetron sputtering method which has lower dielectric constant (ϵ_{BTO} $\sim$40) [7] compared to the

crystalline BTO thin films deposited by MBE or MOCVD method. However, sputtered BTO films also have a comparatively lower refractive index ($n_{BTO} = 1.85$) at 1550 nm wavelength which ensures optical mode confinement in the LN waveguide core region [6]. Besides, the required deposition temperature for amorphous sputtered BTO thin film is much lower compared to the MBE or MOCVD method (typically below 200°C) which is compatible with pre-exisitng metal layers [6], [7], [36]. Therefore, RF magnetron sputtering deposition method should be preferred over that other deposition methods. Secondly, etching of BTO thin film is extremely difficult since pure physical etching techniques are normally used for etching BTO [34]. This may cause the damage of underlying layers. Hence, standard E-beam lithography followed by lift-off of sputtered BTO thin film is preferred for patterning the BTO thin film. Although the deposition of thicker BTO film using an RF magnetron sputter system is quite challenging, it can still be achieved at the cost of longer deposition time. Also, the lift-off process of thicker BTO thin films is quite challenging, but using thick bilayer of E-beam resists the lift-off process can be optimized for thicker BTO films. Nevertheless, with the progress in fabrication techniques we believe that the challenges faced by our proposed modulator structure will eventually be solved that will allow great improvement in the device performances.

REFERENCES

[1] E. L. Wooten et al., "A review of lithium niobate modulators for fiber-optic communications systems," *IEEE J. Sel. Topics Quantum Electron.*, vol. 6, no. 1, pp. 69–82, Jan./Feb. 2000.

[2] R. V. Schmidt and I. P. Kaminow, "Metal–diffused optical waveguides in $LiNbO_3$," *Appl. Phys. Lett.*, vol. 25, no. 8, pp. 458–460, Oct. 1974.

[3] X. Xiao, M. Li, L. Wang, D. Chen, Q. Yang, and S. Yu, "High speed silicon photonic modulators," in *Proc. Opt. Fiber Commun. Conf.*, 2017, paper Tu2H.1.

[4] A. Khilo, C. M. Sorace, and F. X. Kärtner, "Broadband linearized silicon modulator," *Opt. Exp.*, vol. 19, pp. 4485–4500, 2011.

[5] C. Kieninger et al., "Silicon-organic hybrid (SOH) Mach-Zehnder modulators for 100 GBd PAM4 signaling with sub-1 dB phase-shifter loss," *Opt. Exp.*, vol. 28, pp. 24693–24707, 2020.

[6] S. Ummethala et al., "Hybrid electro-optic modulator combining silicon photonic slot waveguides with high-k radio-frequency slotlines," *Optica*, vol. 8, pp. 511–519, 2021.

[7] S. Ummethala et al., "Capacitively coupled silicon-organic hybrid modulator for 200 Gbit/s PAM-4 signaling," in *Proc. Conf. Lasers Electro-Opt.*,, 2019, paper JTh5B.2.

[8] R. G. Walker, "High-speed III-V semiconductor intensity modulators," *IEEE J. Quantum Electron.*, vol. 27, no. 3, pp. 654–667, Mar. 1991.

[9] Y. Ogiso et al., "Ultra-high bandwidth InP IQ modulator for beyond 100-GBd transmission," in *Proc. Opt. Fiber Commun. Conf. Exhib.*, 2019, pp. 1–3.

[10] M. G. Wood et al., "Gigahertz speed operation of Epsilon-near-zero silicon photonic modulators," *Optica*, vol. 5, pp. 233–236, 2018.

[11] Y. Huang et al., "High-bandwidth Si/In_2O_3 hybrid plasmonic waveguide modulator," *APL Photon.*, vol. 7, no. 5, 2022, Art. no. 051301.

[12] D. S. Zemtsov et al., "Plasmon-assisted Si-ITO integrated electro-optical rib-shape modulator," *J. Lightw. Technol.*, vol. 41, no. 19, pp. 6310–6314, Oct. 2023.

[13] M. Burla et al., "500 GHz plasmonic Mach-Zehnder modulator enabling sub-THz microwave photonics," *Apl Photon.*, vol. 4, no. 5, 2019, Art. no. 056106.

[14] S. Ummethala, et al., "THz-to-optical conversion in wireless communications using an ultra-broadband plasmonic modulator," *Nature Photon.*, vol. 13, no. 8, pp. 519–524, 2019.

[15] G. Poberaj, H. Hu, W. Sohler, and P. Gunter, "Lithium niobate on insulator (LNOI) for micro-photonic devices," *Laser Photon. Rev.*, vol. 6, no. 4, pp. 488–503, 2012.

[16] M. Zhang, C. Wang, R. Cheng, A. Shams-Ansari, and M. Lončar, "Monolithic ultra-high-Q lithium niobate microring resonator," *Optica*, vol. 4, pp. 1536–1537, 2017.

[17] C. Wang et al., "Integrated lithium niobate electro-optic modulators operating at CMOS-compatible voltages," *Nature*, vol. 562, pp. 101–104, 2018.

[18] P. Kharel, C. Reimer, K. Luke, L. He, and M. Zhang, "Breaking voltage–bandwidth limits in integrated lithium niobate modulators using micro-structured electrodes," *Optica*, vol. 8, pp. 357–363, 2021.

[19] A. S. Alam and J. S. Aitchison, "Low half-wave-voltage lithium niobate modulator using high-k dielectric material cladding," in *Proc. Optica Adv. Photon. Congr.*, 2022, paper JTu2A.9.

[20] M. Zhang, C. Wang, P. Kharel, D. Zhu, and M. Lončar, "Integrated lithium niobate electro-optic modulators: When performance meets scalability," *Optica*, vol. 8, pp. 652–667, 2021.

[21] N. Chen, K. Lou, Y. Yu, X. He, and T. Chu, "High-efficiency electro-optic modulator on thin-film lithium niobate with high-permittivity cladding," 2023, *arXiv:2304.06946*.

[22] J. Kischkat et al., "Mid-infrared optical properties of thin films of aluminum oxide, titanium dioxide, silicon dioxide, aluminum nitride, and silicon nitride," *Appl Opt.*, vol. 51, no. 28, pp. 6789–98, Oct. 2012.

[23] J. P. Reynard et al., "Integration of fluorine-doped silicon oxide in copper pilot line for 0.12-m technology," *Microelectron. Eng.*, vol. 60, 2002, Art. no. 113.

[24] R. E. Stephens and I. H. Malitson, "Index of refraction of magnesium oxide," *J. Res. Nat. Bur. Standards*, vol. 49, pp. 249–252, 1952.

[25] M.A. Subramanian et al., "Dielectric constants of BeO, MgO, and CaO using the two-terminal method," *Phys. Chem. Minerals*, vol. 16, pp. 741–746, 1989.

[26] A. Niskanen, K. Arstila, M. Ritala, and M. Leskelä, "Low-temperature deposition of aluminum oxide by radical enhanced atomic layer deposition," *J. Electrochem. Soc.*, vol. 152, 2005, Art. no. F90.

[27] X. Liu et al., "Low half-wave-voltage, ultra-high bandwidththin-film LiNbO3 modulator based on hybrid waveguide and periodic capacitively loaded electrodes," 2021, *arXiv:2103.03684*.

[28] M. M. Abdin, W. J. D. Johnson, J. Wang, and T. M. Weller, "W-band finite ground coplanar waveguide (FG-CPW) using laser enhanced direct-print additive manufacturing (LE-DPAM)," in *Proc. IEEE MTT-S Int. Microw. Symp.*, 2019, pp. 1213–1216.

[29] Y. Liu, H. Li, J. Liu, S. Tan, Q. Lu, and W. Guo, "Low V_π thin-film lithium niobate modulator fabricated with photolithography," *Opt. Exp.*, vol. 29, pp. 6320–6329, 2021.

[30] M. He et al., "High-performance hybrid silicon and lithium niobate Mach–Zehnder modulators for 100 $Gbit.s^{-1}$ and beyond," *Nat. Photon.*, vol. 13, pp. 359–364, 2019.

[31] M. Jin, J. Chen, Y. Sua, P. Kumar, and Y. Huang, "Efficient electro-optical modulation on thin-film lithium niobate," *Opt. Lett.*, vol. 46, pp. 1884–1887, 2021.

[32] A. J. Mercante, P. Yao, S. Shi, G. Schneider, J. Murakowski, and D. W. Prather, "110 GHz CMOS compatible thin film $LiNbO_3$ modulator on silicon," *Opt. Exp.*, vol. 24, pp. 15590–15595, 2016.

[33] T. Hamano, D. J. Towner, and B. W. Wessels, "Relative dielectric constant of epitaxial $BaTiO_3$ thin films in the GHz frequency range," *Appl. Phys. Lett.*, vol. 83, no. 25, pp. 5274–5276, 2003.

[34] S. Abel et al., "Large pockels effect in micro-and nanostructured barium titanate integrated on silicon," *Nature Mater.*, vol. 18, no. 1, pp. 42–47, 2019.

[35] D. J. Towner, J. Ni, T. J. Marks, and B. W. Wessels, "Effects of two-stage deposition on the structure and properties of heteroepitaxial $BaTiO_3$ thin films," *J. Cryst. Growth*, vol. 255, no. 1–2, pp. 107-113, 2003.

[36] A. A. Shariful, "Design, fabrication and characterization of capacitively coupled silicon-organic hybrid modulators," Master Thesis, Karlsruhe Institute of Technology (KIT), Karlsruhe, Germany, 2017.